Original Contribution

Automatic Max-Likelihood Envelope Detection Algorithm for Quantitative High-Frame-Rate Ultrasound for Neonatal Brain Monitoring

Anna J. Kortenbout [a], Sophie Costerus [b], Jeroen Dudink [c], Nico de Jong [a,d], Jurgen C. de Graaff [e,f,g], Hendrik J. Vos [a,d], Johan G. Bosch [a,*]

[a] Biomedical Engineering, Department of Cardiology, University Medical Center Rotterdam, Erasmus MC, Rotterdam, The Netherlands
[b] Department of Pediatric Surgery, University Medical Center Rotterdam, Erasmus MC, Rotterdam, The Netherlands
[c] Department of Neonatology, Wilhelmina Children's Hospital, University Medical Center Utrecht, Utrecht, The Netherlands
[d] Department of Imaging Physics, Medical Imaging, Faculty of Applied Sciences, Delft University of Technology, Delft, The Netherlands
[e] Department of Anesthesiology, University Medical Center Rotterdam, Erasmus MC, Rotterdam, The Netherlands
[f] Department of Anesthesiology, Erasmus MC, Goes, The Netherlands
[g] Department of Anesthesiology, Weill Cornell Medicine, New York, NY, USA

Objective: Post-operative brain injury in neonates may result from disturbed cerebral perfusion, but accurate peri-operative monitoring is lacking. High-frame-rate (HFR) cerebral ultrasound could visualize and quantify flow in all detectable vessels using spectral Doppler; however, automated quantification in small vessels is challenging because of low signal amplitude. We have developed an automatic envelope detection algorithm for HFR pulsed wave spectral Doppler signals, enabling neonatal brain quantitative parameter maps during and after surgery.
Methods: HFR ultrasound data from high-risk neonatal surgeries were recorded with a custom HFR mode (frame rate = 1000 Hz) on a Zonare ZS3 system. A pulsed wave Doppler spectrogram was calculated for each pixel containing blood flow in the image, and spectral peak velocity was tracked using a max-likelihood estimation algorithm of signal and noise regions in the spectrogram, where the most likely cross-over point marks the blood flow velocity. The resulting peak systolic velocity (PSV), end-diastolic velocity (EDV) and resistivity index (RI) were compared with other detection schemes, manual tracking and RIs from regular pulsed wave Doppler measurements in 10 neonates.
Results: Envelope detection was successful in both high- and low-quality arterial and venous flow spectrograms. Our technique had the lowest root mean square error for EDV, PSV and RI (0.46 cm/s, 0.53 cm/s and 0.15, respectively) when compared with manual tracking. There was good agreement between the clinical pulsed wave Doppler RI and HFR measurement with a mean difference of 0.07.
Conclusion: The max-likelihood algorithm is a promising approach to accurate, automated cerebral blood flow monitoring with HFR imaging in neonates.

Introduction

Surgery in neonates poses a risk factor for brain injury, which may impair neurodevelopment later in life [1−3]. These brain injuries might be triggered by a disturbance of cerebral blood flow (CBF) in combination with impaired autoregulation [4,5]. Currently, anesthesiologists attempting to optimize CBF during surgery rely on standard monitoring techniques to track heart rate, blood pressure, capillary refill, blood lactate and pH and urine production. However, these markers of CBF lack sensitivity to detect and monitor altered cerebral perfusion [6].

Cerebral ultrasound in neonates using color Doppler or directional power Doppler (DPD) enables sensitive vessel visualization, while pulsed wave spectral Doppler (PWD) quantifies cerebral blood flow velocity (CFBV) in single arteries/veins. PWD uses the Doppler equation

to convert the local spectrum of Doppler frequencies into flow velocities as a function of time, the so-called spectrogram [7]. Although Doppler flow patterns in major cerebral arteries (most commonly the anterior cerebral artery) are often used in neonatal intensive care units to detect brain injury, low frame rates in traditional ultrasound machines limit simultaneous visualization and quantification [8,9]. High-frame-rate (HFR) ultrasound, with more than 1000 frames/s, offers high-resolution imaging and spectral velocity for all pixels, potentially enabling monitoring of cerebral perfusion [10]. Recently, several ultrasound system vendors have implemented clinical or custom HFR options in their devices, such as Supersonic Imagine's Aixplorer [11], GE's Vivid E-9 [12] and Mindray's Zonare ZS3 [13].

Demene et al. [10] were the first to investigate neonatal brain HFR ultrasound quantitatively, creating 2-D resistivity index (RI) maps by

* Corresponding author. Biomedical Engineering, Department of Cardiology, Erasmus MC, Dr. Molewaterplein 60, 3000 CA Rotterdam, The Netherlands.
E-mail address: j.bosch@erasmusmc.nl (J.G. Bosch).

calculating the mean Doppler frequency over time instead of detecting the envelope. However, this mean velocity technique may be sensitive to wall filters, as reported in tissue Doppler imaging [14]. Moreover, spectral noise might give a bias in the estimation. Another study employing HFR ultrasound to investigate the neonatal brain investigated global cerebral blood volume across multiple brain regions during cardiac surgery [15]. However, in that study individual velocities within arteries and veins were not considered. In a different study, which used the single-element NeoDoppler probe, cerebral blood flow velocity was monitored during neonatal non-cardiac surgery, yet this was constrained to only a single, central cylindrical area of the brain [16].

A robust spectral Doppler envelope estimation algorithm is crucial for deriving quantitative information on local velocity and 2-D parameter maps. Various envelope estimation techniques for clinical PWD analysis have been developed, but many are susceptible to poor signal-to-noise ratio (SNR) [17−22]. These approaches rely on threshold crossing, where the maximum frequency is located as a specific percentage of the integrated power spectrum. In these methods, the integrated spectrum is strongly influenced by noise at the far end of the spectrum [17−22]. Kathpalia et al.'s [21] optimized signal noise slope intersection method (oSNSI) provided a more robust maximum velocity estimation but is likely not suitable in low-flow conditions or with HFR ultrasound, where the velocity spectrogram characteristics are less favorable.

To obtain envelope velocity-derived quantitative results, we developed a new, robust automatic spectral envelope estimation algorithm. This algorithm provides parameters in every blood flow pixel in the imaging plane such as peak systolic velocity (PSV), end-diastolic velocity (EDV), and RI. We hypothesize that our envelope detection algorithm enables vascular parameter imaging with a high spatial and temporal resolution for trans-fontanelle imaging in neonates, paving the way for future real-time perfusion monitoring.

Methods

Rationale

As the HFR data are obtained with unfocused plane wave ultrasound in an area with vessels with varying size, diameter and velocity, the spectrograms obtained have strong variations in characteristics, including SNR. Our proposed algorithm intends to adapt to the properties of each local spectrogram. A valid spectrogram contains both signal and noise, where the blood velocity signal is found at the lower Doppler frequencies and the noise is found at all frequencies, yet with lower power density. As both the blood signal and the noise in the spectrograms are often specklelike, a simple power threshold separation will not work well. We adopt a max-likelihood classification approach for separating signal from background (noise), the automatic max-likelihood spectral envelope detection (AMLED) (Fig. 1). A max-likelihood approach has been reported to perform well in ultrasound data with noise and speckle structures [23,24]; however, it has not been applied for spectral envelope detection to our knowledge.
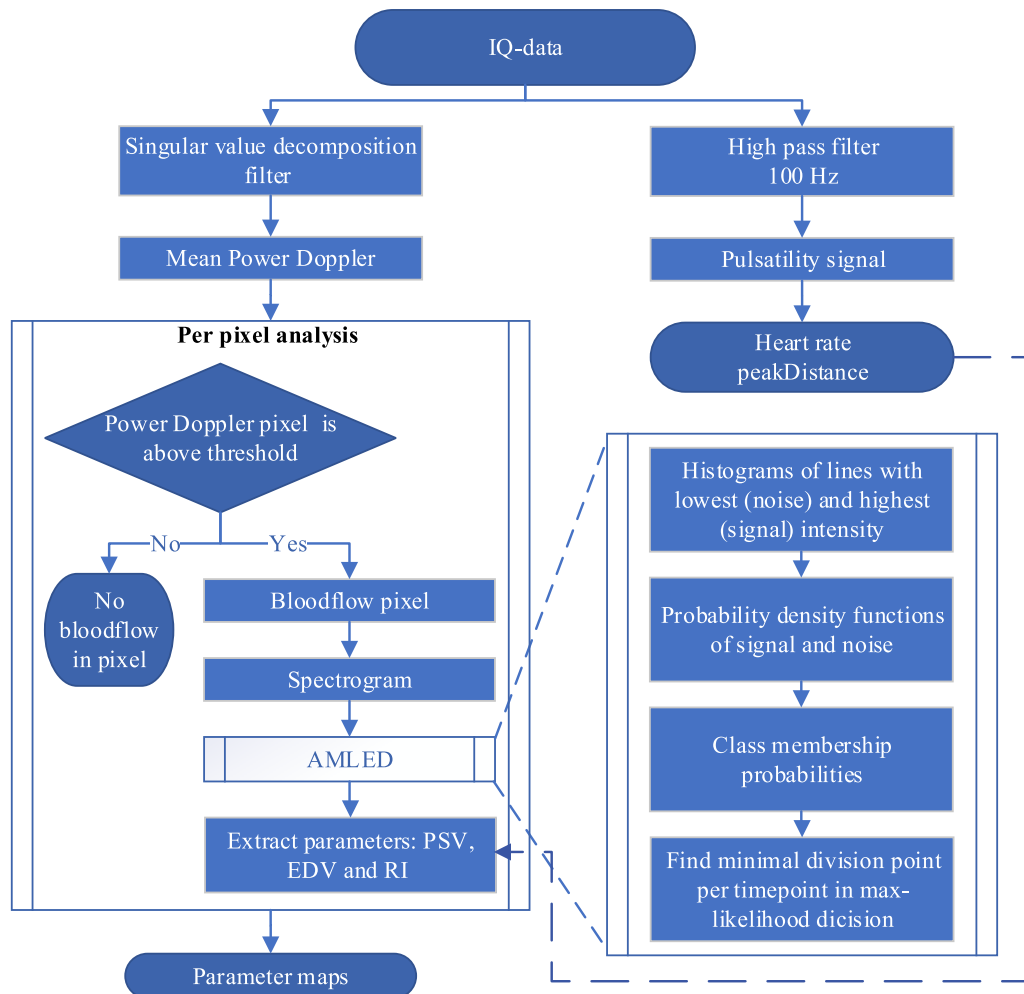

Figure 1. Flowchart of IQ-data analysis with automatic max-likelihood envelope estimation algorithm (AMLED). EDV, end-diastolic velocity; IQ, in-phase and quadrature; PSV, peak systolic velocity; RI, resistivity index.
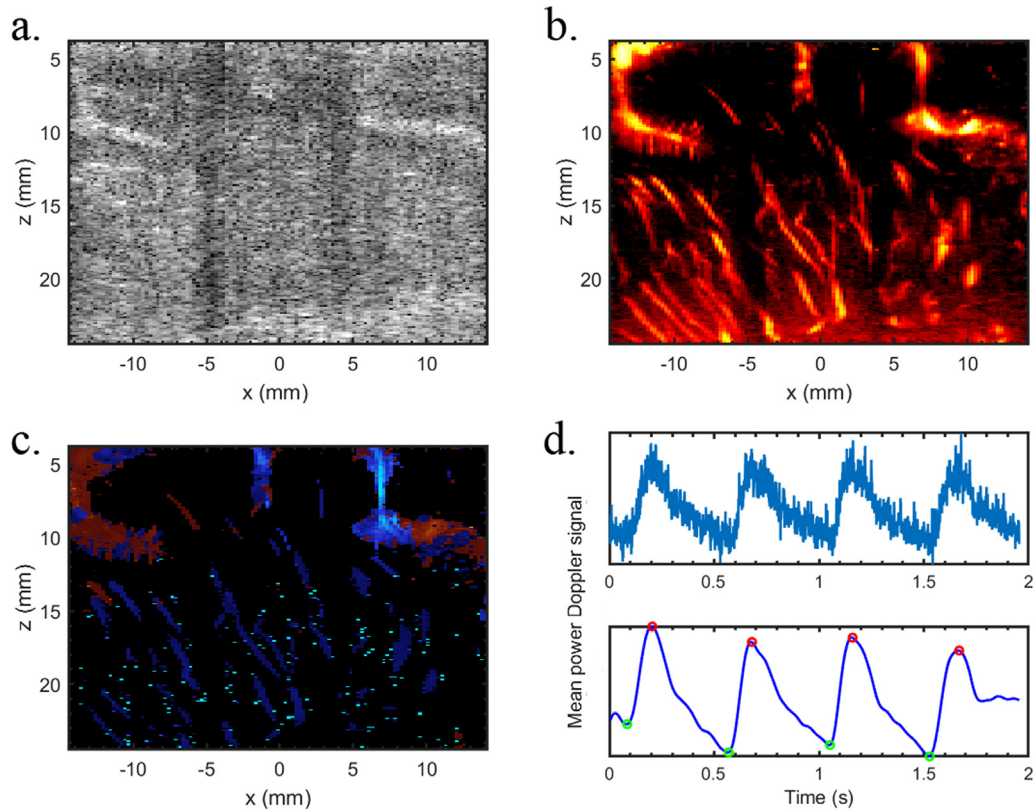
Figure 2. Data preparation steps. (a) The beamformed B-mode data. (b) Power Doppler data after smoothing and singular value decomposition filtering on the in-phase and quadrature data. (c) Directional power Doppler. *Red* indicates dominant flow toward the probe, and *blue,* away from the probe. (d) Slow-time high-pass filtered average time signal of all pixels, indicating the overall pulsatility (top). The timing of systolic peaks (*red dots*) and end-diastolic valleys (*green dots*) are added to the smoothed curve (bottom).

Data acquisition

The ultrasound recordings were obtained with a clinical ultrasound machine, the Zonare ZS3 (Mindray Innovation Center, San Jose, CA, USA) with a high-frequency linear probe (L20-5) at a center frequency f_c of 11 MHz. Data were collected and beamformed in base-band-demodulated in-phase/quadrature (IQ) format, each frame having 250 axial and 115 lateral pixels covering an image width of 30 mm and a depth of 25 mm. During each measurement, a total of 2000 IQ frames were recorded at a frame rate of 1000 Hz.

Data preparation

Figure 2a is a typical example of the B-mode image. Yet, for all processing steps described in the following, the original IQ data were smoothed using a spatiotemporal Gaussian filter with a $3 \times 3 \times 3$ (axial $\times$ lateral $\times$ temporal) kernel size to reduce noise. Singular value decomposition (SVD) was then used on these smoothed IQ frames to remove static tissue signal. A low-rank threshold selection algorithm was applied to determine the cutoff between tissue and blood flow SVD ranks [25,26].

A high-quality power Doppler image (Fig. 2b) is calculated by one-lag autocorrelation of the SVD-filtered IQ data and averaging over all frames, with the sign of the phase shift used to determine the direction of flow for each blood pixel, yielding the directional power Doppler image (Fig. 2c). A threshold at −45 dB was applied mainly to preserve blood flow pixels; these pixels are used for further spectral Doppler processing.

By filtering of the original IQ data with a slow-time high-pass filter at 100 Hz and calculating the average time intensity over all pixels, a general cerebral blood flow pulsatility signal was derived (Fig. 2d). This

allowed us to calculate the heart rate and derive the timing of the systolic peaks and end-diastolic valleys.

The spectrogram (power spectral density [PSD]) for each blood flow pixel was obtained by applying a fast Fourier transform (FFT) to the IQ signal over a slow-time period using a temporal window of 50 frames and an overlap of 40 frames, resulting in an effective sampling rate F_s of 100 spectra/s (Fig. 3a). The spectrogram represents time on the horizontal axis and Doppler frequency on the vertical axis, with the local brightness value representing signal power within the corresponding frequency bin.

The regular Doppler equation illustrates the relationship between each Doppler frequency f_D in the spectrogram and the Doppler velocity (V_D):

$$V_D = \frac{f_D \cdot c_t}{2 f_c} \tag{1}$$

where the c_t is 1540 m/s and center frequency f_c is 11 MHz.

The direction of the dominant velocity is determined by locating the maximum signal intensity of the spectrogram's average over time. For the purpose of imaging the neonatal brain, we assume unidirectional flow, and only one direction is further analyzed. Baseline shifting was performed to reduce the effect of wrap-around (Fig. 3b). The unwrapped PSD $I(t,v)$ with v between 0 and $2v_{max}$ was converted into a 40 dB logarithmic scale represented in 256 intensity levels i.

AMLED

As each image pixel will contain a mix of different flow and tissue velocities, the pixel's spectrogram represents the distribution of velocities at that pixel for each time point. Velocity bins above the actually occurring maximum velocity will contain mainly noise and appear with low intensity value. The maximum velocity that contains significant
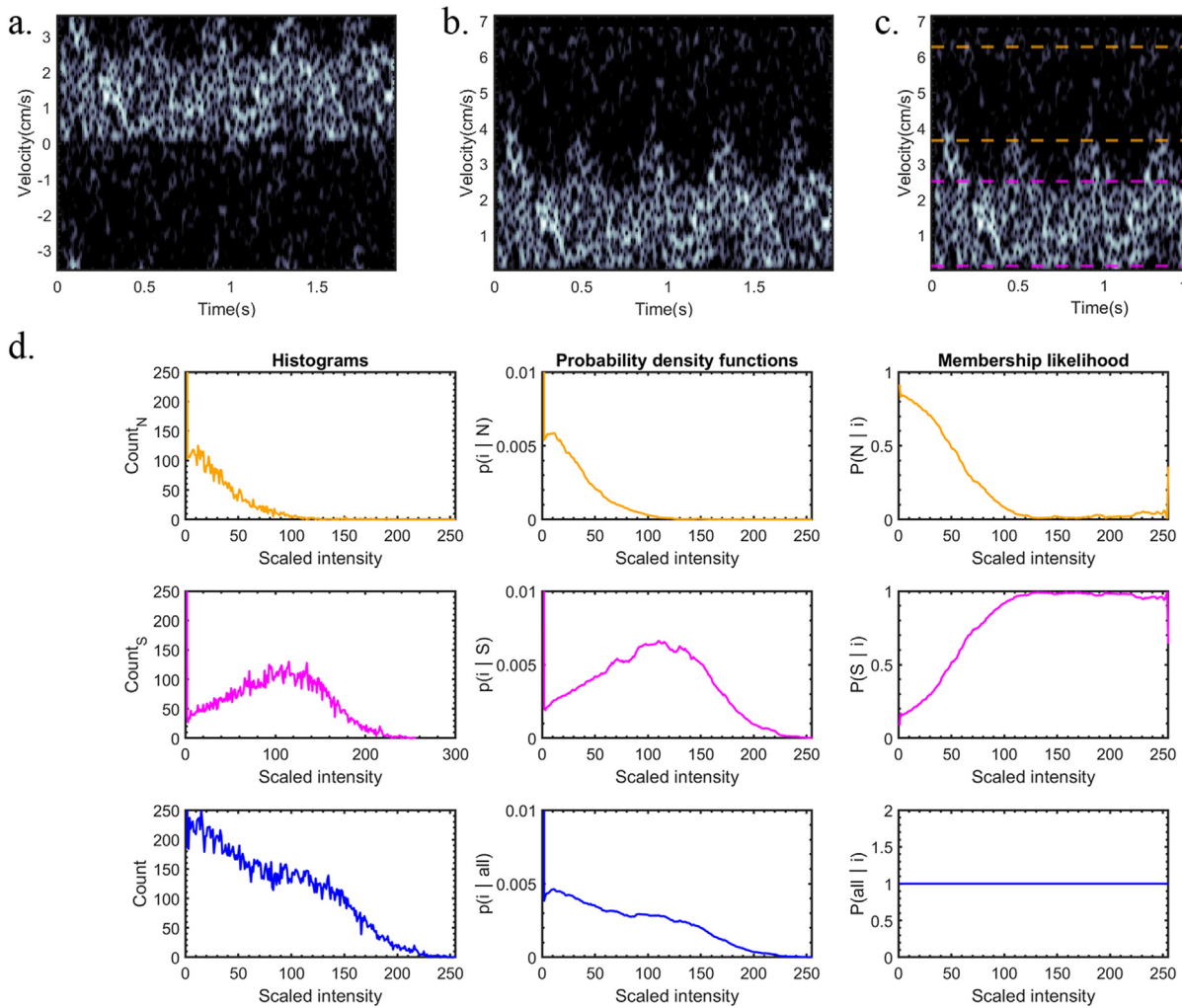
Figure 3. Spectrogram processing. (a) Spectrogram. (b) Unwrapped spectrogram in the positive direction. (c) The area between the *purple dashed lines* represents the detected signal band, and the area between the *orange dashed lines* indicates the noise band. (d) From left to right: histograms, probability density functions (*p(i)*) and membership likelihood (*P(i)*) of (top to bottom) noise *N* (*orange*), signal *S* (*purple*) and summed noise and signal (*blue*).

power above the noise is seen as representing the blood vessel's central velocity. To acquire an envelope of the spectrogram, a velocity envelope point $V_e(t)$ needs to be determined for every time point t. This envelope point is found at the division point between spectral signal and spectral noise.

This segmentation is performed by first identifying the spectrogram rows (velocities) with the highest and lowest average intensity, associated with pure signal and noise, respectively. Then we identify adjacent rows, with an average intensity within 20% of this noise minimum (Fig. 3c, between the *orange dashed lines*) or signal maximum (Fig. 3c, between the *purple dashed lines*). Then, we create histograms $H_s(i)$, $H_n(i)$ (Fig. 3d, left) of the intensities (*i*) for all pixels in the signal and noise rows and initialize the probability density function (PDF) $p(i|S)$, $p(i|N)$ for both regions (Fig. 3d, middle), as well as prior probabilities $p(S)$ for signal and $p(N)$ for noise based on the numbers of rows classified as such. Using Bayes' rule [27], we calculate class membership probabilities $P(S|i)$ and $P(N|i)$ (Fig. 3d, right) with eqns (2) and (3) for each intensity (*i*):

$$P(S|i) = p(i|S) * p(S)/p(i) \tag{2}$$

$$P(N|i) = p(i|N) * p(N)/p(i) \tag{3}$$

We assign additional adjacent rows to the signal and noise regions based on the row's average class membership, and then update all PDFs,

prior probabilities and class membership probabilities. With these final PDFs and prior probabilities, the envelope position $V_e(t)$ for each time point t in the spectrogram (time point t indicated by *azure line* in Fig. 4a) is determined using a maximum-likelihood decision based on the joint probability density function, articulated in eqn (4). We expect signal membership below and noise membership above the envelope. By calculating the sum of negative log-likelihoods for signal $NLL_S = -\log P(S|i)$ below and noise NLL_N membership above each possible partitioning point, the optimal envelope position $V_e(t)$ is identified as the point with the lowest sum (Fig. 4b):

$$V_e(t) = \mathrm{argmin}(V_e)\left(\sum_0^{V_e} NLL_s(t,v) + \sum_{V_e}^{V_{max}} NLL_N(t,v)\right) \tag{4}$$

Furthermore, for the next time point, new prior estimates ($p(S)$, $p(N)$) are updated based on the V_e of the previous time point ($V_e(t-1)$).

Envelope post-processing and parameter extraction

A robust spectral envelope was obtained by excluding time points with insufficient signal quality. Time points with max spectral power below 30% of the mean overall power were excluded. For temporary signal dropouts, the envelope was interpolated. If more than five consecutive time points were excluded, the envelope for these points was removed from the analysis.
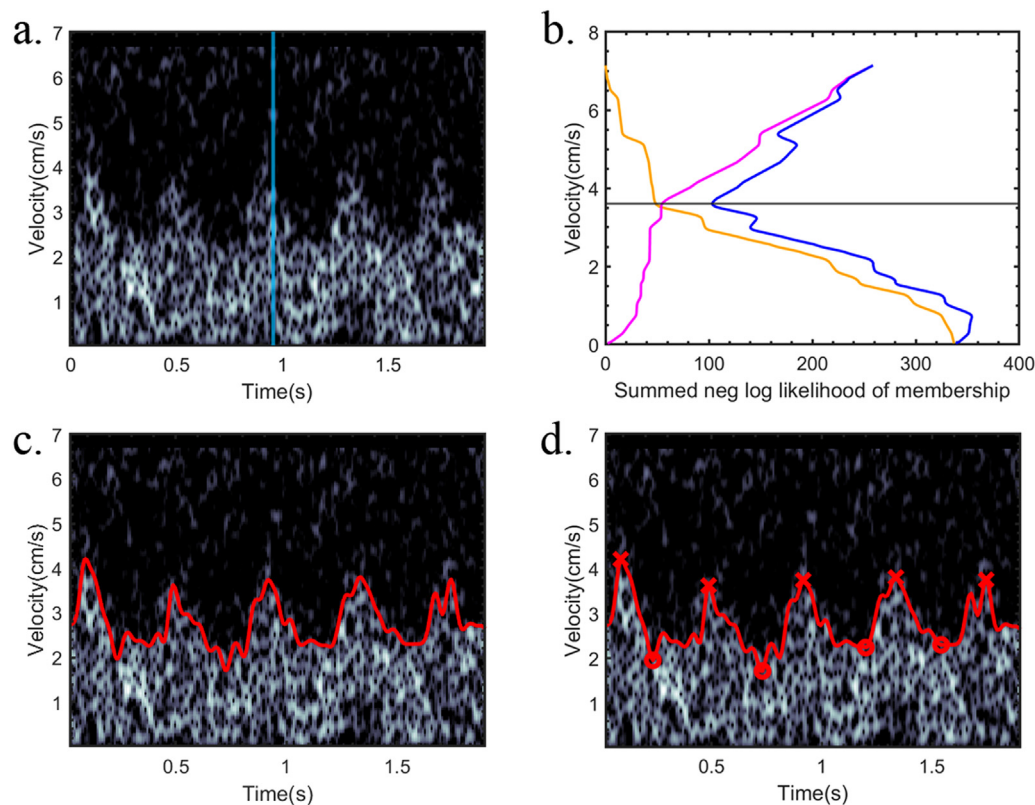
Figure 4. Envelope detection and extrema analysis. (a) *Azure line* indicates the time point that is investigated. (b) Summed negative log likelihoods of signal below candidate point (*purple*), noise above (*orange*) and summed line (*blue*). The best envelope point is found where the summed line is minimal. (c) In *red* is the detected envelope. (d) The detected envelope with red crosses for peak systolic velocity and red *dots* for end-diastolic velocity.

The resulting envelope was low-pass filtered with a cutoff $H = 24 \cdot HR / F_s$ where HR is the heart rate, in beats/second, obtained from the global pulsatility signal, and the factor 24 was empirically determined to maintain the general trend of the spectrogram while removing outliers. The final envelope can be seen in Figure 4c.

The PSV and EDV are identified by detecting peaks and valleys, local maxima and minima in the envelope signal with a minimum peak distance of 80% of the distance between peaks in the global pulsatility signal (Fig. 4d). RI was calculated with the following equation:

$$RI = \frac{PSV - EDV}{PSV} \qquad (5)$$

Evaluation of the AMLED algorithm

To evaluate our method and test the robustness of the detected spectral envelopes with a wide range of SNRs, we used the clinical data obtained in a prospective, observational, feasibility study where we performed transfontanellar clinical PWD and HFR ultrasound in 10 neonates before, during and after surgical treatment of two major congenital anomalies. Institutional research board approval (Medical Ethical Committee Erasmus Medical Centre, MEC 2017-145, amendment feasibility study, February 13, 2019) and signed informed consent were obtained from both parents before start of measurements. The methods and results of the clinical ultrasound measurements were previously published and discussed by Costerus et al. [28]. After a clinical measurement, the probe was held stable and the machine was switched to the custom HFR mode.

We selected 30 arterial (15 low arterial flow [PSV < 2.5 cm/s], 15 high arterial flow) and 15 venous spectrograms from that study. These were representative spectrograms having varying velocities and SNRs and were manually selected from a set of ~1000 spectrograms generated by randomly selecting blood flow pixels in 22 HFR data sets of five neonates. To evaluate the performance of the AMLED algorithm, its results were compared with those obtained from two other envelope estimation techniques, the oSNSI of Kathpalia et al. [21] and mean velocity approach (V_{mean}) [10]. The comparison was made by comparing the parameters (EDV, PSV and RI) derived from the envelopes with those obtained from manual detection. Two independent observers (A.J.K. and J.G.B.) manually selected peaks and valleys in each spectrogram. The observers were instructed to select a specific number of peaks (PSV) and valleys (EDV) based on the pre-determined heart rate and number of cardiac cycles.

The oSNSI method [21] is summarized as follows. For each time point, the cumulative power spectrum is calculated from the PSD and normalized. A signal region, a noise region and the envelope cutoff position V_e are identified in this spectrum based on the local slope of the integrated power spectrum.

The intensity-weighted average velocity of the PSD, V_{mean} was calculated as described by Demene et al. [10]. It should be noted that this mean velocity will always be lower than the V_e of our technique that searches for maximum velocities. Yet, V_{mean} would vary in a similar way as V_e, and a similar RI value can be expected from its peaks and valleys.

To compare RI values of the HFR mode and the RI found with clinical PWD, the same pial artery as investigated with clinical PWD was investigated in the HFR mode. The mean RI was used for the comparison with the RI of the clinical PWD [28].

Lastly, to verify correctness of implementation of all three methods, we tested AMLED alongside V_{mean} and oSNSI on simulated HFR ultrasound data of a carotid *in silico* flow phantom [29] with known ground-truth velocities, spanning one cardiac cycle, with the simulation parameters as previously detailed in Han et al. [30].
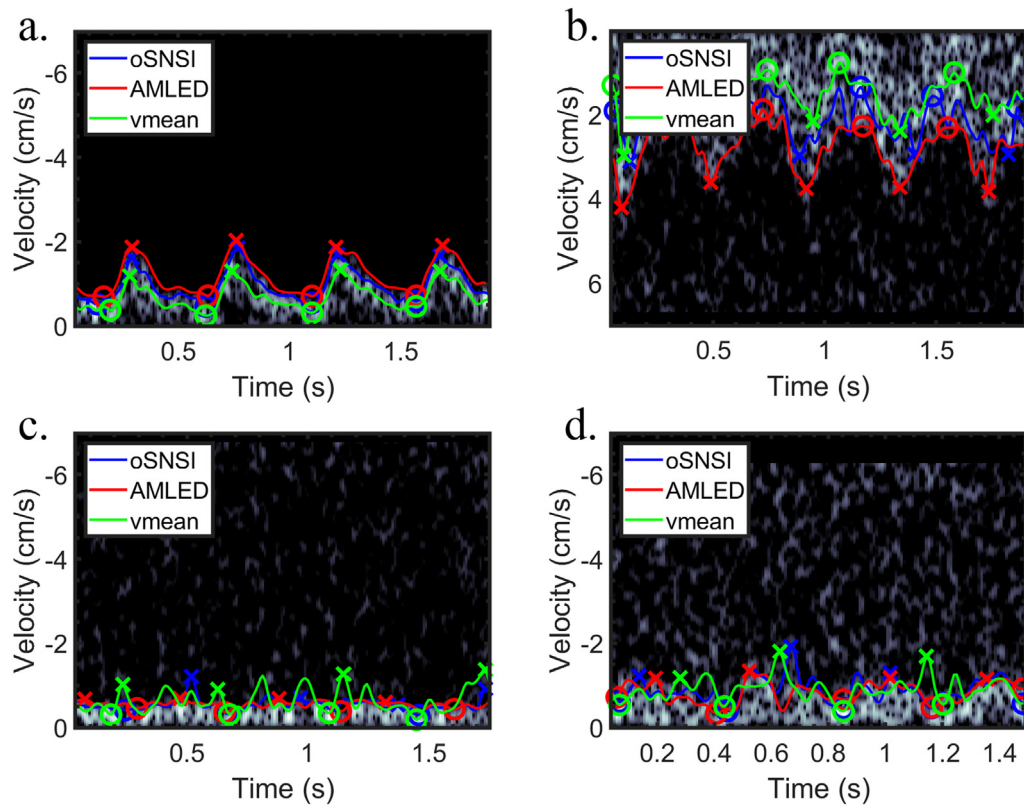
Figure 5. Four spectrograms depicting the performance of three different envelope techniques: automatic max-likelihood envelope estimation algorithm (AMLED, *red*), optimized signal−noise slope intersection (oSNSI, *blue*) and mean velocity (V_{mean}, *green*), under varying signal-to-noise ratio (SNR) conditions. (a) High SNR scenario, arterial. (b) Low SNR arterial blood flow signal. (c) Lower SNR venous signal. (d) Noisy arterial signal.

Statistical analysis

Parameter data obtained from manual detection and the envelope techniques were analyzed using absolute velocity values and are expressed as the mean with standard deviation. The envelopes of the spectrogram derived from the simulated carotid flow data, calculated using the three algorithms, were compared with the ground truth maximum velocity trace. Estimation errors (mean absolute differences) were subsequently calculated and compared. Inter-rater agreement of manual detection between observers was calculated with the intraclass correlation coefficient (ICC). The inter-rater agreement was sufficient (ICC > 0.75) and the PSV, EDV and RI were averaged over the two observers.

Agreement between parameters calculated with the various envelope detection methods and the manual selection was evaluated with Bland −Altman plots [31]. The limits of agreement were set to ±1.96 × SD. A paired-sample *t*-test was used to compare the mean difference between envelope techniques and manual detection. The significance level was set to 0.05. Root mean square errors (RMSE) were calculated as well. Agreement between RI values of the HFR mode and RI of clinical PWD was also assessed with Bland−Altman plots [31].

Statistical analysis was performed with MATLAB (MathWorks MATLAB R2022b, Natick, MA, USA).

Results

General algorithm performance

In Figure 5 are four distinct spectrograms, featuring the AMLED (*red*), oSNSI (*blue*) and V_{mean} (*green*) techniques, alongside parameter values in Table 1. In high-SNR scenarios (Fig. 5a), all techniques perform well, with AMLED giving the highest values and V_{mean} the lowest, while

providing a comparable RI. Figure 5b features a lower SNR arterial blood flow signal, where oSNSI underestimates the envelope, while V_{mean} remains the lowest but has a comparable RI. Figure 5c illustrates a venous signal with lower SNR, where oSNSI and V_{mean} become chaotic, identifying points outside the signal region, but AMLED demonstrates better noise tolerance. Figure 5d features a noisy, low-velocity arterial signal where manual detection is still possible, but all techniques struggle to identify the correct envelope. Nevertheless, AMLED still tracks the spectral signal most consistently. Additionally, in Table 1, AMLED has the lowest standard deviation for EDV and PSV, with the exception of EDV in Figure 5d.

Manual investigation

The mean absolute difference between the two investigators was minor for all parameters, with standard errors for PSV, EDV and RI of 0.004 cm/s, 0.002 cm/s and 0.001, respectively. The results are illustrated in Figure 6. ICC was 1.00 for PSV and EDV and 0.88 for RI. The mean of all parameters selected by the two observers was calculated and used as ground truth for further comparison of envelope detections.

Comparison with other envelope detection algorithms

The max-likelihood envelope detection algorithm, the oSNSI method and V_{mean} were compared with the results from manual tracking. Figure 7 illustrates the agreement between the envelope tracking methods and manual tracking. Note that for comparison between V_{mean} and manual tracking (of V_{max}) only the Bland−Altman plot of RI holds relevance; for EDV and PSV, a considerable difference is expected between V_{mean} and V_{max}; these plots are included for completeness only. With oSNSI, a slight underestimation of both EDV and PSV is observed,

Table 1
Parameter values of example spectrograms of Figure 5

	Manual	oSNSI	V_{mean}	AMLED
Arterial 5a				
EDV (cm/s)	−0.69 (0.06)	−0.54 (0.05)	−0.36 (0.09)	−0.72 (0.01)
PSV (cm/s)	−1.94 (0.06)	−1.74 (0.11)	−1.30 (0.07)	−1.96 (0.07)
Resistivity index	0.64	0.69	0.72	0.63
Arterial 5b				
EDV (cm/s)	2.43 (0.08)	1.53 (0.37)	1.07 (0.27)	2.11 (0.21)
PSV (cm/s)	4.1 (0.12)	2.85 (0.32)	2.25 (0.46)	3.82 (0.23)
Resistivity index	0.40	0.46	0.52	0.45
Venous 5c				
EDV (cm/s)	−0.53 (0.06)	−0.36 (0.06)	−0.30 (0.07)	−0.42 (0.04)
PSV (cm/s)	−0.74 (0.06)	−0.83 (0.26)	−1.16 (0.21)	−0.67 (0.04)
Resistivity index	0.28	0.57	0.75	0.37
Arterial 5d				
EDV (cm/s)	−0.89 (0.09)	−0.52 (0.09)	−0.51 (0.07)	−0.65 (0.23)
PSV (cm/s)	−1.39 (0.08)	−1.70 (0.45)	−1.47 (0.38)	−1.25 (0.09)
Resistivity index	0.36	0.70	0.65	0.48

EDV and PSV values are expressed as the mean (standard deviation).
AMLED, automatic max-likelihood envelope estimation algorithm; EDV, end-diastolic velocity; oSNSI, optimized signal noise slope intersection; PSV, peak systolic velocity; V_{mean}, mean velocity.

consistent with the examples provided in Figure 5. As seen in Table 2, AMLED has the lowest mean difference and RMSE compared with manual tracking.

Calculation times per envelope trace were 0.33 s for oSNSI, 0.08 for V_{mean} and 0.13 for AMLED on a regular desktop PC. To create parameter maps more quickly, these calculation times could be considerably improved by optimizing code or using parallel computing.

Clinical example of monitoring during surgery

In total, 69 HFR measurements of 10 neonates were performed and analyzed. The RI of one pial artery, calculated in the clinical low-frame-rate PWD, was compared with the RI as measured in the same pial artery in the HFR measurement. Overall, the RIs of 47 of 69 measurements could be compared. The selected artery in 15 measurements had higher flow velocities beyond the limits measurable with our HFR ultrasound (>10 cm/s, PRF = 1000 Hz). This flow velocity could be measured by adjusting the PRF for the clinical PWD; however, with the fixed frame rate of the HFR ultrasound of 1000 Hz and center frequency of 11 MHz, the Doppler trace was aliased. In seven measurements, the selected artery in the LFR measurement could not be found in the HFR measurement, and thus, these were excluded. The RI was found to be in good agreement between the two measurements, as illustrated by the Bland

−Altman plot (Fig. 8) with a mean difference of −0.07 and a low RMSE of 0.1.

After application of the AMLED algorithm, EDV, PSV and RI maps of each patient were generated at different time points during surgery, highlighting arteries with high flow velocities and high RIs, possibly indicating arterial structures, where the veins exhibit lower velocities and RIs. In one patient given as an example here (Fig. 9), the impact of the clinical use of norepinephrine infusion on brain perfusion was observed. The infusion caused an increase in both PSV and EDV and a decrease in RI, which later returned to its initial value or even increased.

Simulated data

Figure 10 illustrates the simulated spectrogram with the ground truth maximum velocity trace and the envelopes calculated by AMLED, oSNSI and V_{mean}. The estimation errors were 15.0%, 15.1% and 25.7%, respectively, confirming correct behavior on idealized data.

Discussion

In this article, we have described an automatic spectral envelope estimation algorithm for HFR Doppler ultrasound. We found that
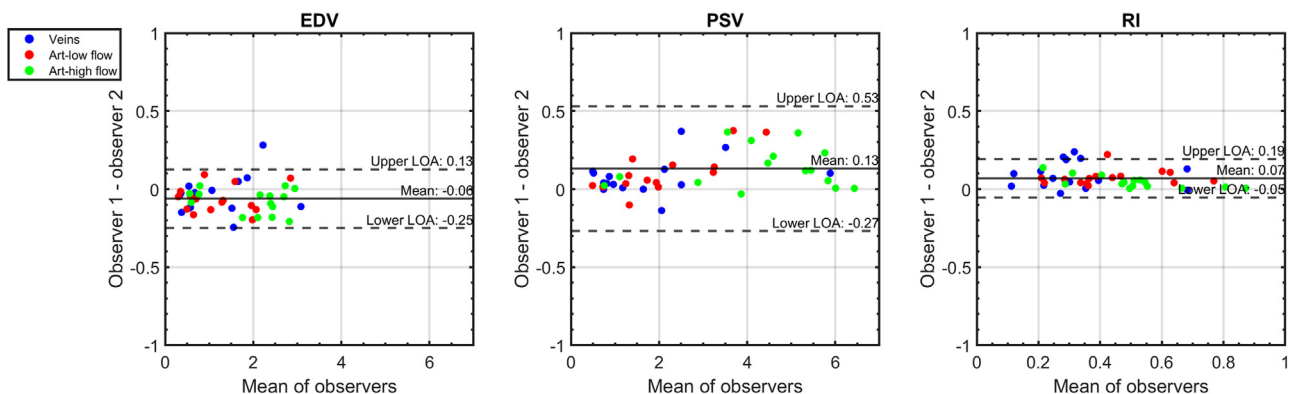

Figure 6. Bland−Altman plots for the manual parameter selection of the two observers. The y-axis is observer 1 − observer 2, and the x-axis is the mean of the observers. *Red points* indicate low arterial flow, *green points* indicate high arterial flow and *blue points* indicate venous flow.
EDV, end-diastolic velocity; LOA, limits of agreement; PSV, peak-systolic velocity; RI, resistivity index.
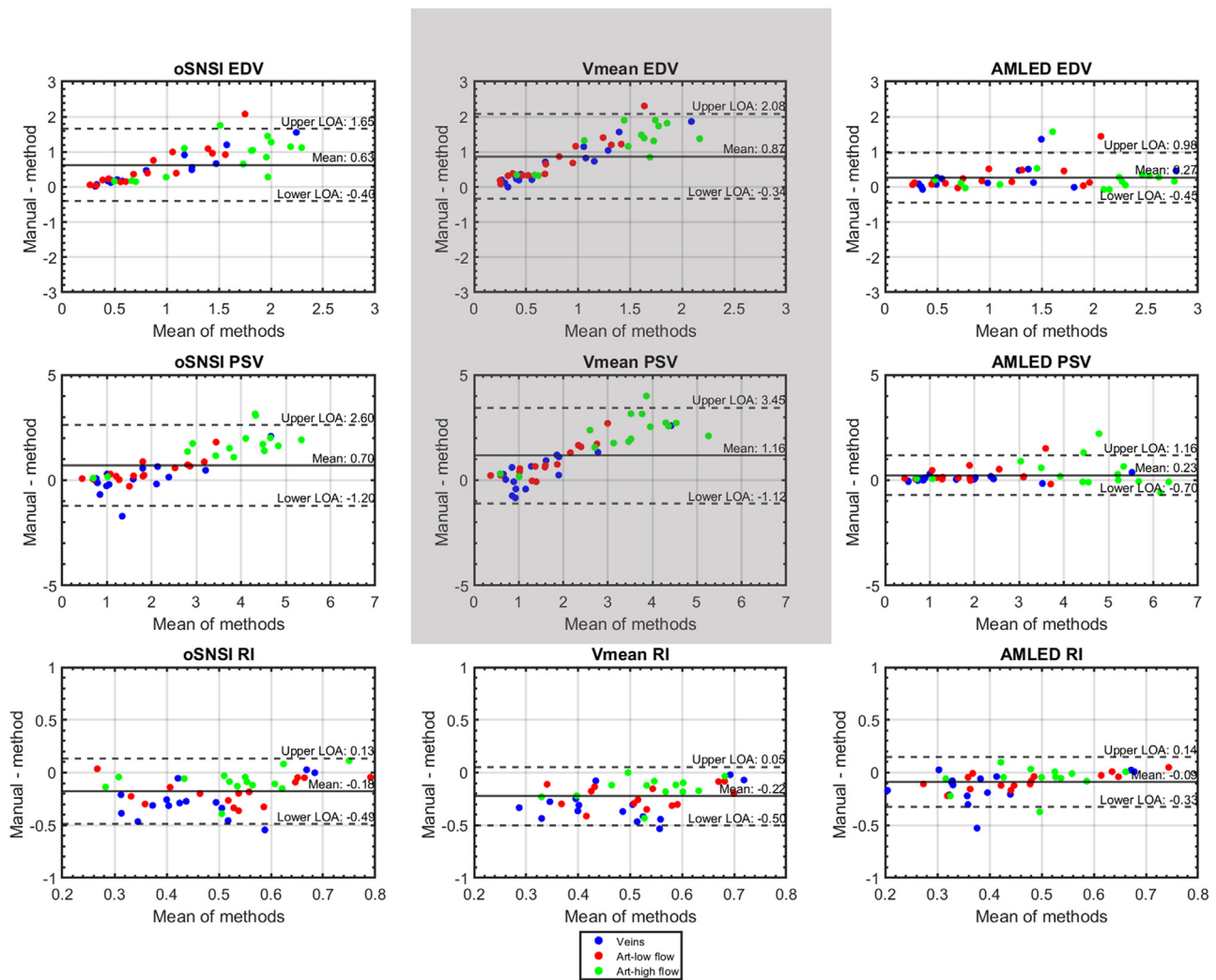
Figure 7. Bland−Altman plots for all envelope methods compared with manual selection. The y-axis is manual selection − envelope method, and the x-axis is the mean of manual and envelope detection. Note that comparison between V_{mean} and manual tracking is not relevant for EDV and PSV. AMLED, automatic max-likelihood enve-lope estimation algorithm; EDV, end-diastolic velocity; oSNSI, optimized signal noise slope intersection; PSV, peak-systolic velocity; RI, resistivity index; V_{mean}, mean velocity.

simultaneous quantification and visualization of cortical cerebral blood flow during high-risk neonatal surgery is feasible with HFR ultrasound. The results obtained using this envelope technique were found to be similar to measurements obtained from the same artery using conventional clinical pulsed wave Doppler, with a mean differ-ence of −0.07.

In comparison of the envelope techniques with manual tracking, the AMLED exhibited the smallest mean difference and the lowest RMSE for

all parameters. Consequently, the AMLED method outperformed both the oSNSI method and V_{mean}.

Envelope detection algorithm

Our envelope detection method (AMLED) exhibited robust perfor-mance across a wide range of high- and low-quality spectrograms, encompassing both arterial and venous flow. It should be noted that we

Table 2

Overview of ultrasound parameter mean difference, limits of agreement and root mean square error envelope techniques compared with manual tracking

	oSNSI			V_{mean}			AMLED		
	Mean	LOA	RMSE	Mean	LOA	RMSE	Mean	LOA	RMSE
EDV (cm/s)	0.64	1.05	0.83	0.89	1.23	1.08	0.27	0.73	0.46
PSV (cm/s)	0.68	1.82	1.14	1.14	2.18	1.58	0.24	0.94	0.53
Resistivity index	−0.18	0.31	0.24	−0.22	0.28	0.27	−0.09	0.25	0.15

AMLED, automatic max-likelihood envelope estimation algorithm; EDV, end-diastolic velocity; LOA, limits of agreement; oSNSI, optimized signal noise slope intersection; PSV, peak systolic velocity; V_{mean}, mean velocity.
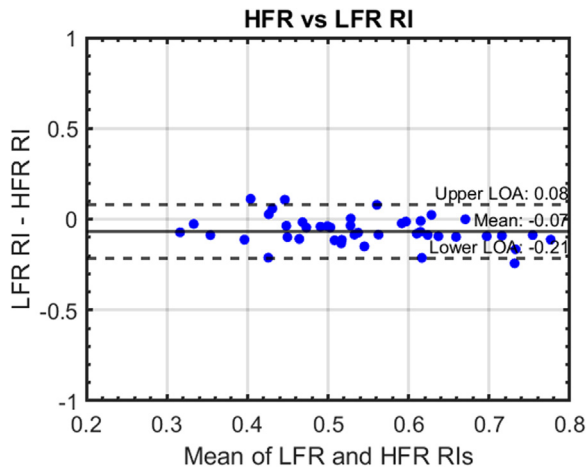
Figure 8. Bland–Altman plot of the RI compared between 47 clinical LFR and HFR measurements in the same artery in 10 neonates. HFR, high frame rate; LFR, low frame rate; LOA, limits of agreement; RI, resistivity index.

did not apply any speckle reduction or noise filtering to the spectrogram data. Our AMLED method proved to give reliable results without such filtering, which might alter the spectrogram envelope. The oSNSI method exhibited an underestimation of PSV and EDV and was more sensitive to noise, even though Kathpalia et al. [21] reported robust estimations for oSNSI with even lower SNR. The likely explanation for this seemingly contradictory finding is that they evaluated their method using simulations, flow phantoms, and clinically obtained spectrograms

from major human arteries, all of which involved very high maximum velocities (≤100 cm/s) and, consequently, spectra with less influence of inherent "speckle." Our data contain many low-velocity vessels where the speckle influence is large.

We also compared our algorithm with V_{mean} used by Demene et al. [10] to create RI maps for HFR Doppler ultrasound. As described in the Methods section, V_{mean} will underestimate peak velocities, and our results indicated that V_{mean} led to underestimation of PSV and EDV but also to overestimation of RI. Although it was expected that this method might provide RI values comparable to those of AMLED, in practice, in spectrograms with poor SNR, it did not perform well.

It is important to note that if a spectrogram is aliased, neither AMLED nor any other method will accurately capture the envelope. In the current mode, the HFR was machine-limited to 1000 frames/s. Theoretically, a pulse repetition frequency up to 30 kHz is possible with a depth range of 25 mm. In our case, we were unable to increase the PRF beyond the machine's limitations. Using a higher frame rate would allow for capturing a broader range of velocities without aliasing. For our specific focus on small periventricular arteries and veins, which exhibit relatively low velocities, a frame rate of 1000 Hz proved sufficient. A more elaborate pre-processing or unwrapping may also be instrumental. Additionally, the algorithm can be extended to acquire envelopes for both the dominant flow direction and the opposite direction. For our clinical application, this was not essential, but it could be beneficial in other scenarios.

HFR parameter map

Our automatic envelope detection algorithm enabled us to generate HFR parameter maps of EDV, PSV and RI of the neonatal brain during
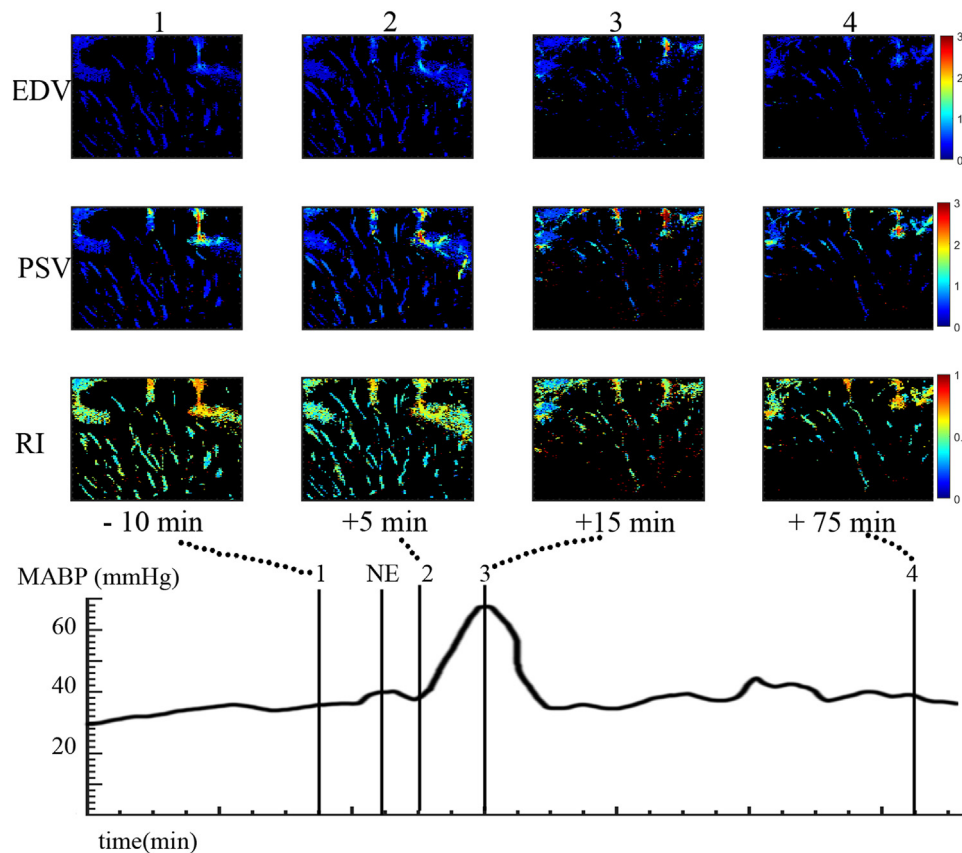

Figure 9. Parameter maps of parasagittal plane of neonate during four different phases of esophagus atresia repair surgery with norepinephrine infusion. EDV, end-diastolic velocity; MABP, mean arterial blood pressure; PSV, peak-systolic velocity; RI, resistivity index.
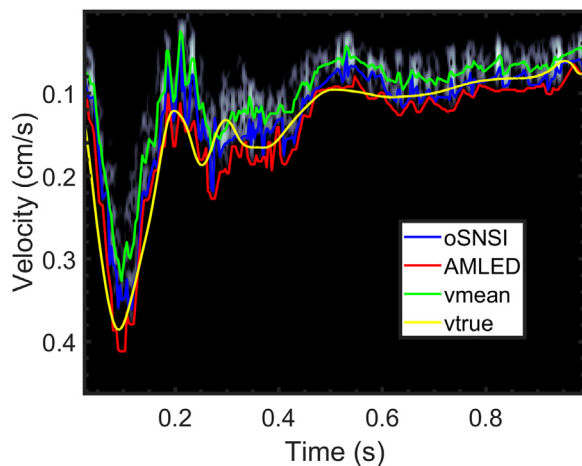
Figure 10. Simulated spectrogram with the ground truth maximum velocity trace in *yellow* and the envelopes calculated by AMLED, oSNSI and V$_{mean}$. AMLED, automatic max-likelihood envelope estimation algorithm; oSNSI, optimized signal noise slope intersection; V_{mean}, mean velocity.

high-risk non-cardiac surgery. Vital parameters during surgery provide poor approximations of brain perfusion in neonates [6]. In one case where incidental norepinephrine infusion was started for clinical use, we observed an overall increase in PSV and EDV, with a more significant effect in EDV, resulting in a decrease in RI. Interestingly, fewer vessels were observed in the measurements after the noradrenalin injection, which might indicate cerebral vessel vasoconstriction [32]. These changes can be explained by the inotropic effects of norepinephrine, which increase peripheral vascular resistance, resulting in less flow in smaller vessels, possibly leading to fewer observed vessels [33]. These findings may have implications for understanding the effects of noradrenalin on cerebral vasculature during surgery. This incidental finding emphasizes the potential of HFR ultrasound to monitor drug effects on brain perfusion.

Clinical implications and future directions

A future improvement would be to provide the HFR analysis in real time, which would further facilitate selection of relevant views and vessels. The fully automated analysis would eventually facilitate hands-off long-duration ultrasound monitoring with, for example, small wearable probes. Future research should expand knowledge on the effect of fluctuation of Doppler parameters during surgery on later observed brain injury, and if the Doppler parameters, next to other vital parameters, can improve peri-operative management on cerebral perfusion.

Conclusion

In this study, we developed a novel automatic envelope detection algorithm for providing quantitative parameter maps of blood flow based on HFR pulsed wave Doppler signals. Our method had low root mean square errors in estimating EDV, PSV and RI, even with varying-quality spectrograms with different flow conditions. Our results suggest that HFR ultrasound has the potential to serve as an additional tool to monitor cerebral perfusion, for example, during major high-risk neonatal surgery.

Conflict of interest

The authors declare no competing interests.

Data availability statement

No consent for public data sharing is given by the participants of this study. Aggregate data may be shared on reasonable request.

References

[1] Leeuwen L, Schiller RM, Rietman AB, van Rosmalen J, Wildschut ED, Houmes RJM, et al. Risk factors of impaired neuropsychologic outcome in school-aged survivors of neonatal critical illness. Crit Care Med 2018;46:401–10.

[2] Stolwijk LJ, Keunen K, de Vries LS, Groenendaal F, van der Zee DC, van Herwaarden MYA, et al. Neonatal surgery for noncardiac congenital anomalies: neonates at risk of brain injury. J Pediatr 2017;182:335–341.e1.

[3] Stolwijk LJ, Lemmers PM, Harmsen M, Groenendaal F, de Vries LS, van der Zee DC, et al. Neurodevelopmental outcomes after neonatal surgery for major noncardiac anomalies. Pediatrics 2016;137:e20151728.

[4] McCann ME, Lee JK, Inder T. Beyond anesthesia toxicity: anesthetic considerations to lessen the risk of neonatal neurological injury. Anesth Analg 2019;129:1354–64.

[5] McCann ME, Schouten AN, Dobija N, Munoz C, Stephenson L, Poussaint TY, et al. Infantile postoperative encephalopathy: perioperative factors as a cause for concern. Pediatrics 2014;133:e751–7.

[6] McCann ME, Schouten AN. Beyond survival: influences of blood pressure, cerebral perfusion and anesthesia on neurodevelopment. Paediatr Anaesth 2014;24:68–73.

[7] Szabo TL. Doppler modes editor. In: Szabo TL, editor. Diagnostic ultrasound imaging: inside out. 2nd ed. Boston: Academic Press; 2014. p. 431–500.

[8] Dudink J, Jeanne Steggerda S, Horsch S. State-of-the-art neonatal cerebral ultrasound: technique and reporting. Pediatr Res 2020;87(Suppl. 1):3–12.

[9] Tanter M, Fink M. Ultrafast imaging in biomedical ultrasound. IEEE Trans Ultrason Ferroelectr Freq Control 2014;61:102–19.

[10] Demene C, Pernot M, Biran V, Alison M, Fink M, Baud O, et al. Ultrafast Doppler reveals the mapping of cerebral vascular resistivity in neonates. J Cereb Blood Flow Metab 2014;34:1009–17.

[11] Bercoff J, Montaldo G, Loupas T, Savery D, Mézière F, Fink M, et al. Ultrafast compound Doppler imaging: providing full blood flow characterization. IEEE Trans Ultrason Ferroelectr Freq Control 2011;58:134–47.

[12] Mawad W, Løvstakken L, Fadnes S, Grønli T, Segers P, Mertens L, et al. Right ventricular flow dynamics in dilated right ventricles: energy loss estimation based on blood speckle tracking echocardiography—a pilot study in children. Ultrasound Med Biol 2021;47:1514–27.

[13] Keijzer LBH, Strachinaru M, Bowen DJ, Geleijnse ML, van der Steen AFW, Bosch JG, et al. Reproducibility of natural shear wave elastography measurements. Ultrasound Med Biol 2019;45:3172–85.

[14] Brekke B, Nilsen LC, Lund J, Torp H, Bjastad T, Amundsen BH, et al. Ultra-high frame rate tissue Doppler imaging. Ultrasound Med Biol 2014;40:222–31.

[15] Aguet J, Fakhari N, Nguyen M, Mertens L, Szabo E, Ertl-Wagner B, et al. Impact of cardiopulmonary bypass on cerebrovascular autoregulation assessed by ultrafast ultrasound imaging. J Physiol 2023;601:1077–93.

[16] Vik SD, Torp H, Jarmund AH, Kiss G, Follestad T, Støen R, et al. Continuous monitoring of cerebral blood flow during general anaesthesia in infants. BJA Open 2023;6:100144.

[17] Mo LY, Yun LC, Cobbold RS. Comparison of four digital maximum frequency estimators for Doppler ultrasound. Ultrasound Med Biol 1988;14:355–63.

[18] Marasek K, Nowicki A. Comparison of the performance of three maximum Doppler frequency estimators coupled with different spectral estimation methods. Ultrasound Med Biol 1994;20:629–38.

[19] Steinman AH, Tavakkoli J, Myers Jr JG, Cobbold RS, Johnston KW. Sources of error in maximum velocity estimation using linear phased-array Doppler systems with steady flow. Ultrasound Med Biol 2001;27:655–64.

[20] Ricci S, Vilkomerson D, Matera R, Tortoli P. Accurate blood peak velocity estimation using spectral models and vector doppler. IEEE Trans Ultrason Ferroelectr Freq Control 2015;62:686–96.

[21] Kathpalia A, Karabiyik Y, Eik-Nes SH, Tegnander E, Ekroll IK, Kiss G, et al. Adaptive spectral envelope estimation for Doppler ultrasound. IEEE Trans Ultrason Ferroelectr Freq Control 2016;63:1825–38.

[22] D'Alessio T. Objective' algorithm for maximum frequency estimation in Doppler spectral analysers. Med Biol Eng Comput 1985;23:63–8.

[23] Sarti A, Corsi C, Mazzini E, Lamberti C. Maximum likelihood segmentation of ultrasound images with Rayleigh distribution. IEEE Trans Ultrason Ferroelectr Freq Control 2005;52:947–60.

[24] Vegas-Sánchez-Ferrero G, Martín-Fernández M, Sanches JM. A gamma mixture model for IVUS imaging. In: Saba L, Sanches JM, Pedro LM, Suri JS, editors. Multi-

modality atherosclerosis imaging and diagnosis. New York: Springer; 2014. p. 155–71.

[25] Demene C, Deffieux T, Pernot M, Osmanski BF, Biran V, Gennisson JL, et al. Spatio-temporal clutter filtering of ultrafast ultrasound data highly increases Doppler and fultrasound sensitivity. IEEE Trans Med Imaging 2015;34:2271–85.

[26] Yu ACH, Lovstakken L. Eigen-based clutter filter design for ultrasound color flow imaging: a review. IEEE Trans Ultrason Ferroelectr Freq Control 2010;57:1096–111.

[27] Bayes M, Price M. An essay towards solving a problem in the doctrine of chances. By the Late Rev. Mr. Bayes, F.R.S. Communicated by Mr. Price, in a letter to John Canton, A.M.F.R.S. Philos Trans 1763;53:370–418.

[28] Costerus SA, Kortenbout AJ, Vos HJ, Govaert P, Tibboel D, Wijnen RMH, et al. Feasibility of Doppler ultrasound for cortical cerebral blood flow velocity monitoring during major non-cardiac surgery of newborns. Front Pediatr 2021;9:656806.

[29] Swillens A, Løvstakken L, Kips J, Torp H, Segers P. Ultrasound simulation of complex flow velocity fields based on computational fluid dynamics. IEEE Trans Ultrason Ferroelectr Freq Control 2009;56:546–56.

[30] Han Y, Segers P, Bosch JG, Voorneveld J. Improving peak velocity estimation accuracy in EchoPIV using anisotropic windows. In: Proc 2022 IEEE Int Ultrason Symp (IUS), Venice, Italy, October 10−13; 2022.

[31] Bland MJ, Altman D. Statistical methods for assessing agreement between two methods of clinical measurement. Lancet 1986;327:307–10.

[32] Froese L, Dian J, Gomez A, Unger B, Zeiler FA. The cerebrovascular response to norepinephrine: a scoping systematic review of the animal and human literature. Pharmacol Res Perspect 2020;8:e00655.

[33] King BD, Sokoloff L, Wechsler RL. The effects of l-epinephrine and l-norepinephrine upon cerebral circulation and metabolism in man. J Clin Invest 1952;31:273–9.